A Modified Active Flyback-Forward Converter derived Isolated Three-Phase Micro-inverter with Artificial Neural Network (ANN)

R.Palanisamy[1] K.Sathiyasekar[2]

[1]*Department of Electrical and Electronics Engineering, M.P. Nachimuthu M.Jaganathan Engineering College,*
Erode – 638112, Tamil Nadu, India
[2] *Department of Electrical and Electronics Engineering, S.A. Engineering College, Poonamallee,*
Chennai – 600077, Tamil Nadu, India
palani6118@yahoo.com

Abstract— A dual boost Modified Active Clamp Flyback Forward Converter (MACFFC) based isolated micro-inverter is presented to provide high boosting gain with reduced switching stress and duty ratio. The proposed system is designed to boost the 24 V PV array output voltages into 400 V, 50 Hz AC which is required for the synchronization of grid. Normally, the flyback boost converter derived micro-inverters offers enhanced power transfer capability between the PV array and grid. The active clamp flyback converter provides single stage boosting with extremely high duty ratio. The proposed system is construed with an inductors and three winding coupled inductor, Voltage Doubler (VD) rectifier and full bridge Voltage Source Inverter (VSI) to enhance the power transfer capability and to increase the conversion efficiency by reducing active and passive components. In addition, a dual input dual output Artificial Neural Network (ANN) is adopted to provide the wide range of control over the transfer of real and reactive power and to provide low Total Harmonic Distortion (THD) at the load. The results of the simulated and experimental models are presented to validate the power transfer capability of the proposed three-phase micro-inverter.

Keywords: Dual Boost Modified Active Clamp Flyback Forward Converter (MACFFC), Artificial Neural Network (ANN), Voltage Doubler (VD) Rectifier, Voltage Source Inverter (VSI), Inner Voltage Control Loop.

1. Introduction

Nowadays, the power generation through the renewable energy sources such as wind, solar, biomass, hydro, geo thermal and tidal have increased due to the growing demand of electricity. Among these the solar power generation system is more popular due its availability, low cost and simplicity. The Photovoltaic (PV) arrays connect with the utility grid is gaining more attention while the power demand is increasing day by day [1]-[3]. Commonly, a number of low voltage PV cells are integrated to improve the output power and voltage of the PV power generating systems. The output voltages of the PV arrays are low during the rainy and partially shadow days. This needs a front end boost converter to step-up the PV array output voltage for the grid-inter connection. The required boost converter should have high boosting gain, high efficiency and small voltage ripple [4] – [6]. There are various topologies are presented, some of them are based on the cascaded DC-DC converters and additional bidirectional DC-DC converters those increases the weight, volume and complexity of the control algorithms [7]-[10]. A single-phase micro-inverter which is constructed with a multi-level buffer and voltage modulator is presented to reduce the size of the DC link capacitor [11]. It helps to enhance the buffering capability between the DC to AC conversion.

Recently solutions based on the coupled inductor and active flyback converters have been extended to grid connected PV systems. The Active Clamp Flyback Forward Converter (ACFFC) provides favorable solution for boosting the low value of PV array output voltage with reduced number of switches and passive elements [12]-[14]. In reference [15], a flyback converter based single-phase single-stage micro-inverter is presented to separate the decoupling capacitor from the PV module. It reduces the required decoupling capacitance and improves the reliability by reducing the power frequency ripple. Fuel cell power generation system with ACFFC is presented to boost 12V DC to 220V AC [16]. The topology utilizes the high boost interleaved soft-switching flyback convert with zero voltage switching to provides single stage boosting for the input voltage. In addition to the flyback converter, an LC low pass filter is adopted to reduce THD of the load voltage. The SEPIC converter operated micro inverter based on single ended primary inductance converter topology with active power decoupling is presented in [17]. Reference [18], presented an improved hybrid control strategy to improve the efficiency and power transfer capability of the interleaved flyback converter based micro-inverter. The reference current calculation of the model has been proposed to estimate the switching and conduction losses of the micro-inverter. In reference [19], an interleaved active clamped forward flyback converter based isolated photovoltaic micro-inverter for stand-alone and grid connected applications are presented to transfer the power generated on the PV array to grid. From the investigation of literature, it is found that the single-stage ACFFC employed isolated micro-inverters are not optimal for the high boost PV power generation system because they have low boosting gain. To overcome the drawback of the conventional interleaved flyback forward converter, a MACFFC converter incorporated isolated micro-inverter is proposed.

In this paper, a dual boost MACFFC based isolated micro-inverter is presented to improve the boosting gain, conversion efficiency and to reduce the number of passive components. In addition with this, a dual input dual output ANN controller incorporated grid side control loop is presented to optimize the transfer of real and reactive power from the PV array. The PI controller based inner voltage control loop maintains the DC–link voltage of the VSI at described level. The simulation and experimental results of the dual boost high gain MACFFC derived micro-inverter have validated the theoretical predictions and power transfer capability of the proposed system. Figure 1 shows the system configuration of the conventional single boost two winding coupled inductor based grid connected micro-inverter.

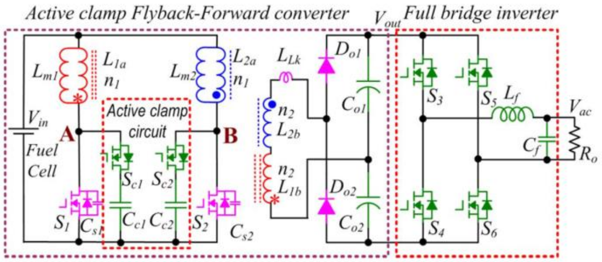

Figure1. System configuration of singe boost ACFFC with two coupled inductor

2. Circuit Configuration and Modes of Operation

The circuit topology of the proposed dual boost MACFFC based three-phase micro-inverter is presented in Figure 2. The proposed micro-inverter is derived from the conventional single stage active clamp forward flyback converter which is shown in Figure 1. The proposed dual boost high step-up active clamp flyback forward converter based isolated micro-inverter consists of dual boost active clamp flyback circuit, three winding coupled inductor, VD rectifier, Voltage Source Inverter (VSI), Neural Network based grid side control and inner voltage control loop as illustrated in Figure 2. In the proposed circuit topology, the active flyback converter provides dual boost with high voltage gain than the conventional flyback converter. In addition with this, PQ theory controller incorporated with the ANN helps to increase the reliability and to decrease the THD content of the voltage supplied to the grid. The following sub section deals with the different operating modes of the proposed MACFFC derived three-phase micro-inverter.

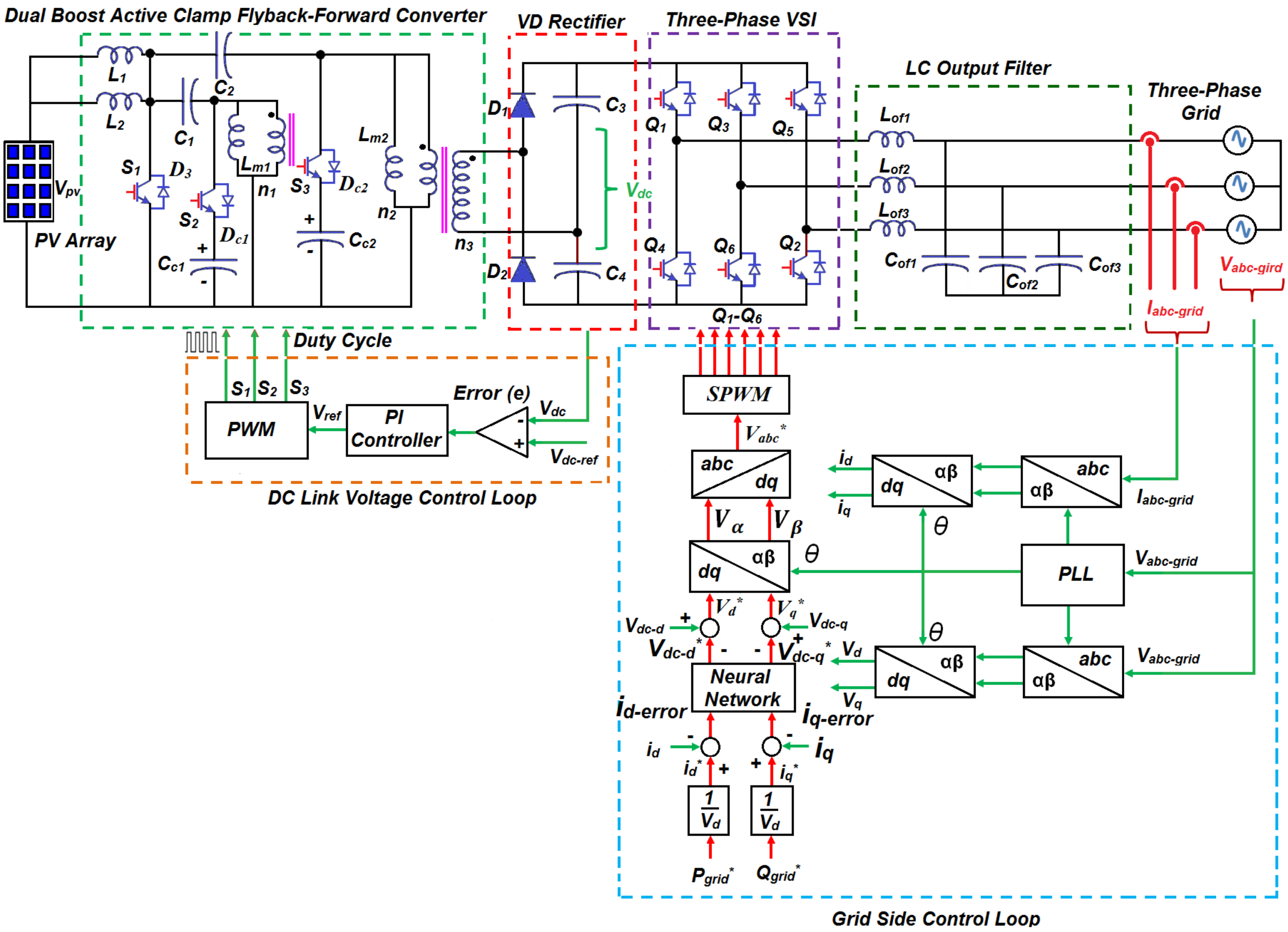

Figure 2. Circuit topology of the proposed MACFFC based dual boost high gain three-phase micro-inverter

2.1 Operational Analysis of the proposed micro inverter

In this section, the six different modes of the proposed dual boost MACFFC based micro-inverter are presented. There are three high frequency switches are utilized. The surplus energy of the mutual inductance L_{m1} and L_{m2} are stored in the decoupling capacitors C_{c1} and C_{c2} through the diodes. This helps to increase the efficiency of the proposed micro-inverter. The circuit diagrams for the six different modes of operation are illustrated in Figure 3. The waveforms of the different operating modes are illustrated in Figure 4.

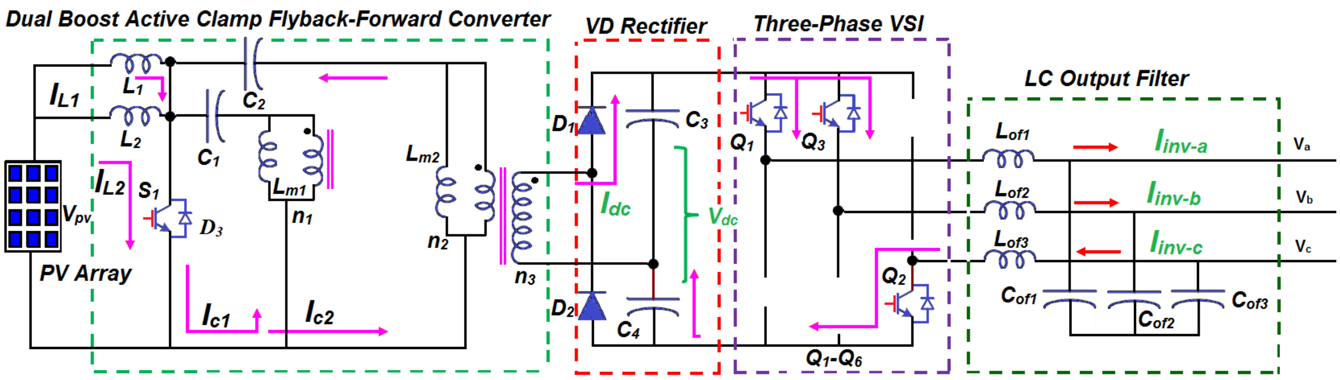

a) Mode 1

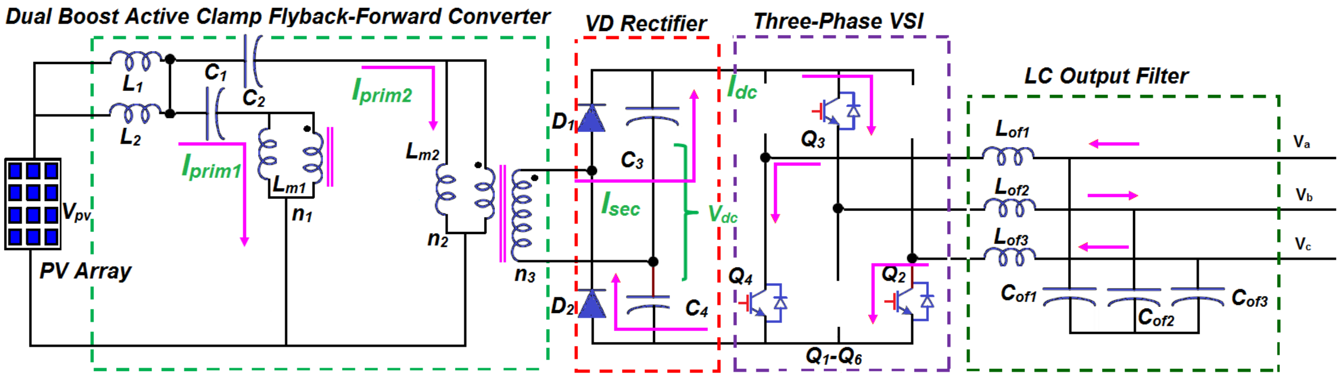

b) Mode 2

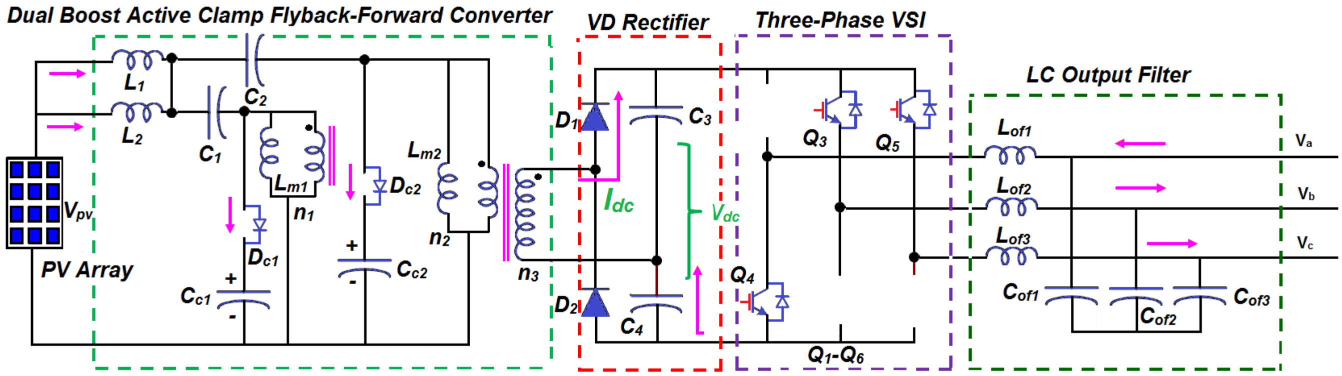

c) Mode 3

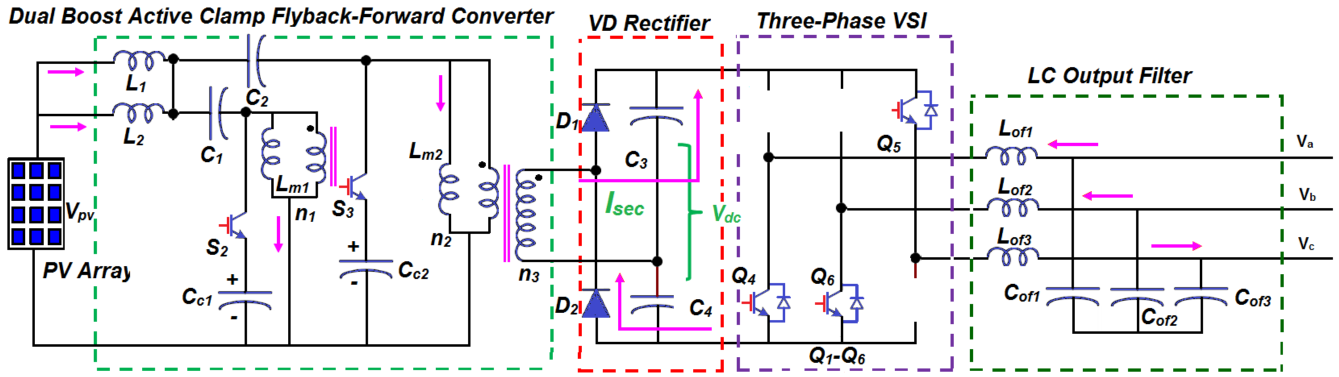

d) Mode 4

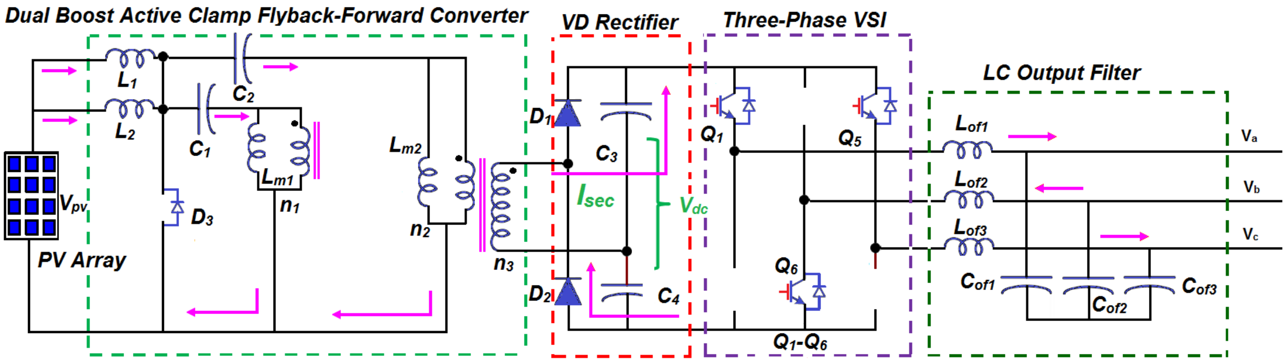

e) Mode 5

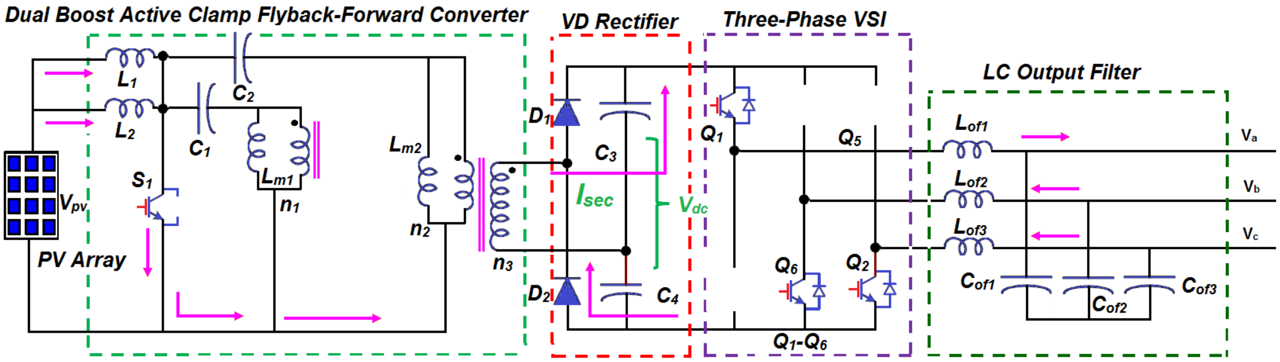

f) Mode 6

Figure 3. Different operating modes of the proposed ACFFC derived three-phase micro-inverter

1) Mode 1 (Interval $t_0 < t < t_1$): This state begins, when the high frequency switch S_1 is turned ON. The input inductors L_1 and L_2 are charged in parallel with the PV array output voltage. The energy stored in the capacitors C_1 and C_2 charges the magnetizing inductors L_{m1} and L_{m2} through S_1. The voltage across the inductor L_1 and L_2 can be expressed as given in Equation (1). The current flowing through the inductor L_1 and L_2 are presented in Equation (2). Assuming the initial state of the inductor as zero. The inverter switches Q_1, Q_2 and Q_3 are in turned ON position to perform the DC-AC conversion and grid inter-connection. The equivalent circuit and current flow path for the Mode 1 is illustrated in Figure 3(a).

$$V_{L1} = L_1\frac{di_{L1}}{dt} = V_{L2} = L_2\frac{di_{L2}}{dt} \tag{1}$$

$$I_{L1}(t) = \frac{V_{pv}(t_1 - t_0)}{L_1} = I_{L2}(t) = \frac{V_{pv}(t_1 - t_0)}{L_2} \tag{2}$$

where, I_{L1} and I_{L2} are the current following through the inductor L_1 and L_2, V_{L1} and V_{L2} are the voltage across the inductor L_1 and L_2 and V_{pv} is the PV array voltage.

2) Mode 2 (Interval $t_1 < t < t_2$): This mode starts when the high frequency switches S_1 and the decoupling clamp switches S_2 and S_3 are turned OFF. The inductors L_1 and L_2 charged during the mode 1 are connected in series with the PV source and the primary of coupled inductor L_1 and L_2 as illustrated in Figure 3 (b). The inductor L_1 and the capacitor C_1 delivers the energy stored to the primary 1 of the coupled inductor. Similarly, the inductor L_2 and the capacitor C_2 discharges the stored energy to the primary 2 of the coupled inductor. The high frequency output voltage of the coupled inductor is rectified through the VD rectifier and the conversion of DC-AC is obtained by VSI. The currents of the inductor L_1 and L_2 and the voltage across the inductors L_1 and L_2 are expressed as given in Equs. (3) – (6). The VSI switches Q_2, Q_3 and Q_4 are turned ON to transfer the power available in the DC link to grid.

$$I_{L1}(t) = \frac{V_{L1}(t_2 - t_1)}{L_1} + I_{L1}(t_1) \quad (3)$$

$$I_{L2}(t) = \frac{V_{L2}(t_2 - t_1)}{L_2} + I_{L2}(t_1) \quad (4)$$

$$V_{L1} = V_{pv} - V_{c1} - \frac{V_{dc}}{n} \quad (5)$$

$$V_{L2} = V_{pv} - V_{c2} - \frac{V_{dc}}{n} \quad (6)$$

Where, V_{c1} and V_{c2} are the voltage across the capacitors C_1 and C_2, respectively, V_{dc} is the DC link voltage and n is the turn's ratio of the three-winding coupled inductor.

3) Mode 3 (intervals $t_2 < t < t_3$): This state begins, when the magnitude of the voltage across the capacitor is enough to forward bias the diodes D_{c1} and D_{c2}. During this interval, the energy stored in the inductors L_1 and L_2 are transferred to the decoupling capacitors C_{c1} and C_{c2} through the diodes D_{c1} and D_{c2} as presented in Figure 3(c). This mode ends when the diodes current D_{c1} and D_{c2} are equal to zero. The diodes D_{c1} and D_{c2} are reverse biased at the end of this mode. The switches Q_3, Q_4 and Q_5 are switched ON to transfer the power from the DC link to gird. The current and voltage of the inductors and capacitors are expressed as

$$I_{L1}(t) = I_{C1}(t) = \frac{V_{L1}(t_2 - t_3)}{L_1} + I_{L1}(t_3) \quad (7)$$

$$I_{L2}(t) = I_{C2}(t) = \frac{V_{L2}(t_2 - t_3)}{L_2} + I_{L2}(t_3) \quad (8)$$

$$V_{L1} = V_{pv} - V_{c1} - V_{Lm1} \quad (9)$$

$$V_{L2} = V_{pv} - V_{c2} - V_{Lm2} \quad (10)$$

where, $I_{c1}(t)$ and $I_{c2}(t)$ are the current following through the capacitors C_1 and C_2, respectively, V_{Lm1} and V_{Lm2} are the voltage across the mutual inductance L_{m1} and L_{m2}.

4) Mode 4 (Intervals $t_3 < t < t_4$): This mode starts when S_2 and S_3 are turned ON as illustrated in Figure 3 (d). The decoupling clamp capacitors C_{c1} and C_{c2} charges L_{m1} and L_{m2} in reverse polarity. The mode continuous till the primary currents of the high frequency transformer reaches the determined value. The DC-AC conversion is carried out by turn-oning the Q_4, Q_5 and Q_6. The voltage and current expressions of the input inductors L_1 and L_2 and the mutual inductance L_{m1} and L_{m2} are expressed as given in Equation (11) – Equation (14).

$$I_{L1}(t) = I_{C1}(t) = \frac{V_{L1}(t_3 - t_4)}{L_1} + I_{L1}(t_4) \quad (11)$$

$$I_{L2}(t) = I_{C2}(t) = \frac{V_{L2}(t_3 - t_4)}{L_2} + I_{L2}(t_4) \quad (12)$$

$$V_{L1} = V_{pv} - V_{c1} - V_{Lm1} \quad (13)$$

$$V_{L2} = V_{pv} - V_{c2} - V_{Lm2} \quad (14)$$

5) Mode 5 (Intervals $t_4 < t < t_5$): When the active clamp switches S_2 and S_3 are turned OFF, the magnetizing inductance L_{m1} and L_{m2} charges the capacitor C_1 and C_2 through the diodes D_3. It increases the voltage of capacitors C_1 and C_2. Figure 3 (e) shows the equivalent circuit and current flow path of this mode. This mode ends when the current flowing through the inductors L_1 and L_2 and the magnetizing inductors L_{m1} and L_{m2} are equal. The current equation of the I_{L1}, I_{L2}, I_{m1} and I_{m2} are presented in Equation (15) and Equation (16).

$$I_{L1}(t) = I_{Lm1}(t) = \frac{V_{L1}(t_4 - t_5)}{L_1} + I_{L1}(t_4) \quad (15)$$

$$I_{L2}(t) = I_{Lm2}(t) = \frac{V_{L2}(t_4 - t_5)}{L_2} + I_{L2}(t_4) \quad (16)$$

6) Mode 6 (Intervals $t_5 < t < t_6$): This mode starts when the switch S_1 is switched ON again as shown in Figure 3(f). The decoupling switches S_2 and S_3 are turned OFF. The inductor L_1 and L_2 gets the charge through the PV array. The energy stored in the capacitors C_1 and C_2 are freewheeled through the primary 1 and primary 2 of the coupled inductor. The inductance current expressions are presented in Equation (17) to Equation (18).

$$I_{L1}(t) = I_{Lm1}(t) = \frac{V_{L1}(t - t_6)}{L_1} + I_{L1}(t_6) \quad (17)$$

$$I_{L2}(t) = I_{Lm2}(t) = \frac{V_{L2}(t - t_6)}{L_2} + I_{L2}(t_6) \quad (18)$$

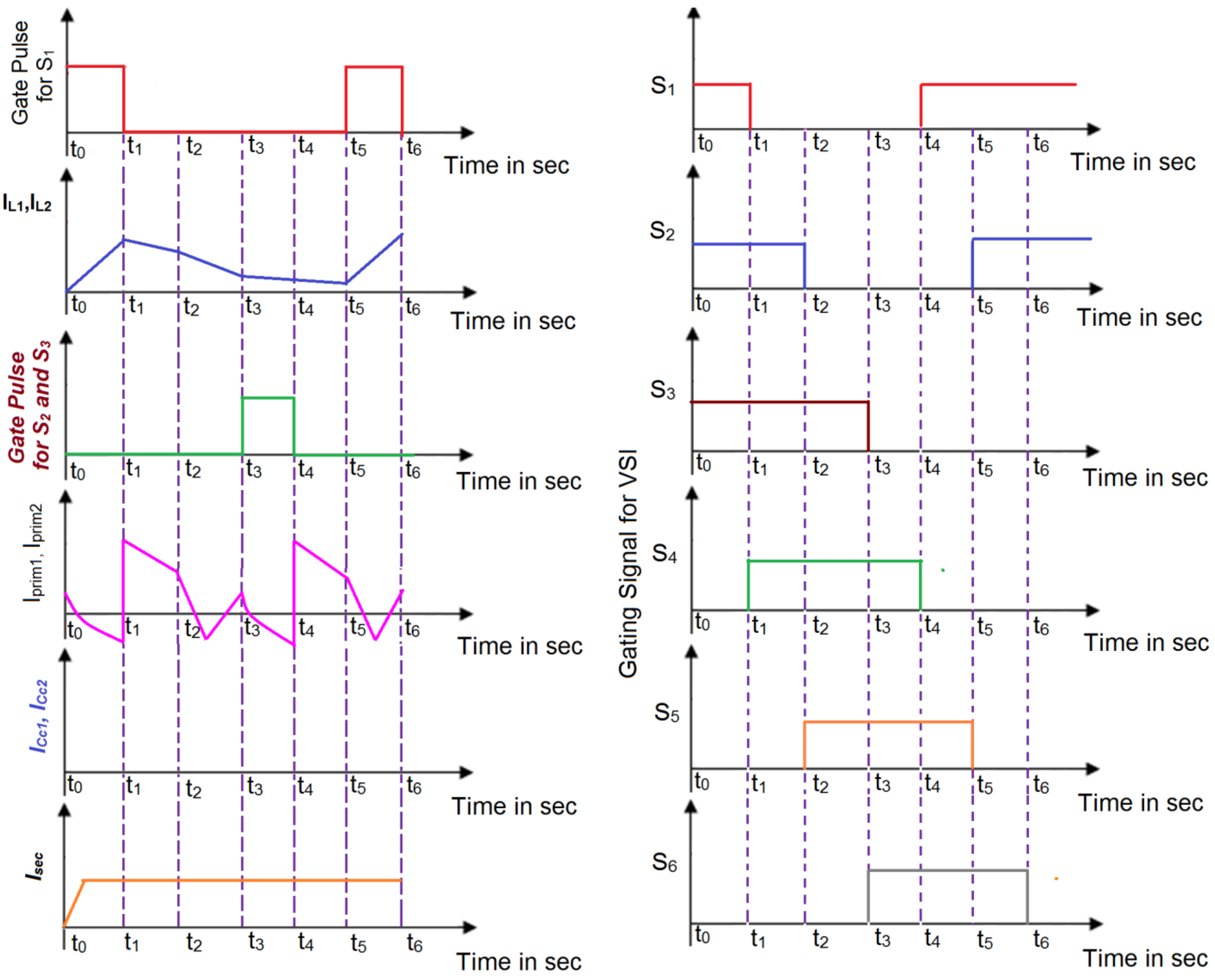

Figure 4. Waveforms of the different operating modes

3. Control Strategy of the Proposed Micro-Inverter

The control strategy of the proposed dual boost MACFFC derived three-phase isolated micro-inverter is constructed with two control loops namely voltage control loop and grid side control loop as presented in Figure 1. The controllers incorporated with the proposed system regulate the DC link voltage and output voltage of the VSI for the synchronization with grid.

3.1 ANN based grid side control

The grid side controller performs two functions: 1) It controls the real and reactive power injected into the grid and 2) Regulates the inverter output voltage at the level required for grid synchronization. Synchronous Reference Frame (SRF) theory with dual input dual output ANN controller is proposed to enhance the stability and to provide the high quality AC to the load. The three-phase real and reactive power supplied into the grid can be expressed as given in Equation (19) and Equation (20).

$$P_{inv} = \sqrt{3}\, V_{inv}\, I_{inv} \cos \emptyset \tag{19}$$

$$Q_{inv} = \sqrt{3}\, V_{inv}\, I_{inv}\, Sin\ \emptyset \tag{20}$$

where, P_{inv} is the real power of the VSI, Q_{inv} is the reactive power of the VSI, V_{inv} output voltage of the VSI, I_{inv} is the inverter output current and ∅ is the angle between V_{inv} and I_{inv}.

The transformations of grid voltage into d-axis and q-axis components are obtained by using the Equs. (21) and (22).

$$\begin{bmatrix} V_\alpha \\ V_\beta \end{bmatrix} = \sqrt{\frac{2}{3}} \begin{bmatrix} 1 & -\frac{1}{2} & -\frac{1}{2} \\ 0 & \frac{\sqrt{3}}{2} & -\sqrt{\frac{3}{2}} \end{bmatrix} \begin{bmatrix} V_{a-grid} \\ V_{b-grid} \\ V_{C-grid} \end{bmatrix} \tag{21}$$

$$\begin{bmatrix} V_d \\ V_q \end{bmatrix} = \begin{bmatrix} \cos(\theta) & \sin(\theta) \\ -\sin(\theta) & \cos(\theta) \end{bmatrix} \begin{bmatrix} V_\alpha \\ V_\beta \end{bmatrix} \tag{22}$$

where, V_{a-grid}, V_{b-grid} and V_{c-grid} are the per phase grid voltages, V_d and V_q are the d-axis and q-axis voltages, I_{a-grid}, I_{b-grid} and I_{c-grid} are the per phase grid voltages and I_d and I_q are the d-axis and q-axis currents.

Similarly, the grid current conversions are obtained by using the Equs. (23) and (24).

$$\begin{bmatrix} I_\alpha \\ I_\beta \end{bmatrix} = \sqrt{\frac{2}{3}} \begin{bmatrix} 1 & -\frac{1}{2} & -\frac{1}{2} \\ 0 & \frac{\sqrt{3}}{2} & -\sqrt{\frac{3}{2}} \end{bmatrix} \begin{bmatrix} I_{a-grid} \\ I_{b-grid} \\ I_{C-grid} \end{bmatrix} \tag{23}$$

$$\begin{bmatrix} I_d \\ I_q \end{bmatrix} = \begin{bmatrix} \cos(\theta) & \sin(\theta) \\ -\sin(\theta) & \cos(\theta) \end{bmatrix} \begin{bmatrix} I_\alpha \\ I_\beta \end{bmatrix} \tag{24}$$

The transformations of rotating frame variables (dq) into stationery frame variables ($\alpha\beta$) are obtained by using the **Equation (25).** Similarly, the Equation (26) transforms the V_{dq} variables to V_{abc}.

$$\begin{bmatrix} V_\alpha \\ V_\beta \end{bmatrix} = \begin{bmatrix} \cos(\theta) & -\sin(\theta) \\ \sin(\theta) & \cos\theta \end{bmatrix} \begin{bmatrix} V_d \\ V_q \end{bmatrix} \tag{25}$$

$$\begin{bmatrix} U_a \\ U_b \\ U_C \end{bmatrix} = \sqrt{\frac{2}{3}} \begin{bmatrix} 1 & 0 \\ -\frac{1}{2} & \frac{\sqrt{3}}{2} \\ -\frac{1}{2} & -\frac{\sqrt{3}}{2} \end{bmatrix} \begin{bmatrix} V_\alpha \\ V_\beta \end{bmatrix} \tag{26}$$

The grid voltage and current measured at the AC bus is transformed into V_d, V_q, I_d and I_q variables. The Phase Locked Loop (PLL) block is utilized to extract the angle θ from the measured grid voltage $V_{abc-grid.}$ The reference d-axis and q-axis currents I_d^* and I_q^* are obtained by the following equations.

$$I_d{}^* = \frac{P^*}{V_d} \tag{27}$$

$$I_q{}^* = \frac{Q^*}{V_d} \tag{28}$$

where, I_d^* is the reference direct axis current, I_q^* is the quadrature axis current and P^* and Q^* are the reference active and reactive power, respectively.

The errors obtained during the comparison of reference d-axis and q-axis parameters with the actual parameter obtained from the grid voltage and current are processed through the dual input dual output ANN controller for the optimal generation of reference components V_d* and V_q^*. The outputs obtained from the NN controller are compared with the V_{dc-d} and V_{dc-q} to produce the V_d* and V_q^*. The outputs of the comparator are given to *dp-αβ* conversion block. The outputs of the *dp-αβ* conversion block are further processed to generate the required gate pulses for the MACFFC through *αβ-abc* transformation. The PWM pulse generator generates the gate pulses required for the switches Q_1 *to* Q_6. In the grid side control, ANN current controller is utilized to process the error signal. The internal configuration of the ANN is illustrated in Figure 5.

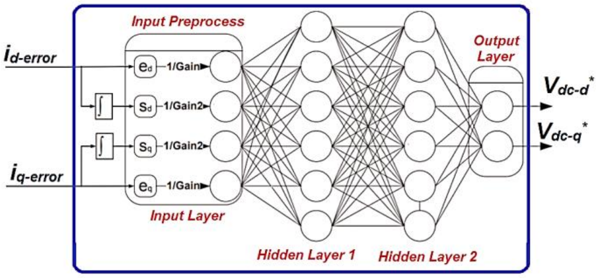

Figure 5. Internal structure of the dual input dual output ANN controller

The ANN is constructed with four layers: input layer, hidden layer 1, hidden layer 2 and output layer. There are four inputs at the input layer as illustrated in Figure 5. Two of the inputs are the error signals obtained from the comparator. The other two input signals are derived by taking integration of the error signals. The integral part of the error signals provides the sum of past errors which helps to prevent the ANN from staying at a non-target value. Further, the four inputs are divided by their respective gain and the output of the input layer is feed forward to the six hidden nodes. Finally, the outputs of the action layers are converted into V_{dc-d}^{*} and V_{dc-q}^{*}.

3.2 DC link voltage control loop

The DC link voltage control loop embedded with proposed isolated micro-inverter regulates the output voltage of the rectifier by adjusting the duty cycle of MACFFC. The voltage control loop is constructed with a voltage comparator, PI controller and PWM pulse generator as presented in Figure 6. The voltage comparator intended to compare the V_{dc} with the reference DC link voltage V_{dc}^{*}. The error (e) obtained by the comparison is fed to PI controller for further action and controls. The processed error signal V_{ref} is applied to the PWM pulse generator. The PWM pulse generator generates the firing pulses for the switches S_1, S_2 and S_3 in accordance with the requirement.

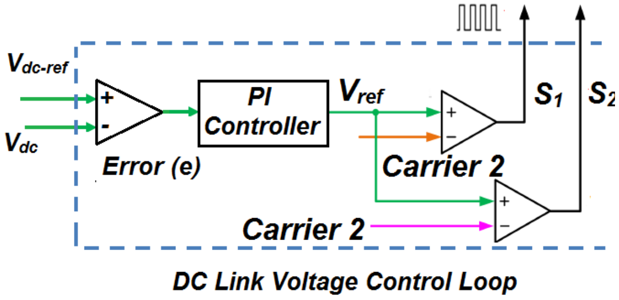

Figure 6. Control Structure of the Inner DC link voltage control

4. Simulation Verification

The simulation model of a 6 KW, 400 V, 50 Hz system is developed to verify the topology and control strategy of the proposed micro-inverter. Simulated model parameters are tabulated in Table 1.

Table 1 Parameters of the Simulated Model

Grid voltage (V_{grid})	400 V	Capacitor C_1 and C_2	18.8 µF
Grid frequency (f_{grid})	50 Hz	Capacitor C_3 and C_4	500 µF
PV panel rated voltage (V_{pv})	12 V	Capacitor C_{c1} and C_{c2}	6.6 µF
Number of Cells	96 Cells	Turns ratio of the coupled inductor	1:10
Open circuit voltage of PV panel	59.01 V	Switching frequency of ACFFC	25 kHz
Short circuit current of PV panel	10.87 A	VSI switching frequency	20 kHz
PV rated power	500 W	Output filter inductance	38 mH
Inductor L_1 and L_2	0.1273 mH	Output filter capacitance	20 µF
Load Resistance	120 Ω / 60Ω	Load Inductance	0.1 mH

The simulation model of the proposed dual boost MACFFC derived micro-inverter is validated under two different case studies. First investigation is carried out under the variable solar irradiation on the PV array with constant load on the grid. For the second investigation, a constant solar irradiation with dynamic load is considered. The DC link voltage of the simulated model is maintained at 600 V to stabilize the output voltage of the three-phase VSI.

4.1 Case 1: Variable Solar Irradiation with Constant Load

During this examination, the solar irradiation applied to the PV array is raised to 1000 W/m^2 at 0.25 sec. The corresponding variation in the PV array output voltage is depicted in Figure 7 (a). Figure 7 shows the PV array voltage, PV array current, PV array power, primary 1 voltage, primary 2 voltage and secondary voltage, DC link voltage and DC link current of the VSI.

In Figure 8, output voltage of the inverter without filter, load voltage, load current, real and reactive power supplied to the grid, THD content of the inverter output voltage before the filter, THD contents of the phase A, THD contents of phase B and THD contents phase C are presented.

From the investigation of case 1, it is observed that the voltage control loop incorporated with the proposed micro-inverter maintains the DC link voltage at 600 V. It is evident that the MACFFC offers high boosting gain for the PV array output voltage. The magnitude of the DC link voltage and the performance of the VSI are not affected with the sudden raise in the PV array output voltage. From the investigation of the simulation results presented in Figure 8 (f) – (h), it is clear that the THD content of the voltage injected into the gird is around 0.30%.

4.2 Case 2: Constant Solar Irradiation with Dynamic Load

The investigation of case 2 is carried out under the variable load conditions with constant solar irradiation on the PV array. The load on the proposed system is increased from 3.3 A to 6.6 A at t=0.25 sec. The output voltage of the PV array, PV array current, PV power, primary 1 voltage, primary 2 voltage, secondary voltage, DC link voltage and DC link current of the proposed system is presented in Figure 9. Figure 10 shows the inverter output voltage before the filter, load voltage, load current, real and reactive power supplied to the load, THD content of the inverter output voltage and THD content of the each phases of the load voltage after the filter.

From the Figure 9 (g), it is observed that a small voltage dip is caused during the sudden rise in the load current. Suddenly, the voltage control loop embedded with the system respond to variation in V_{dc} and increase the duty ratio of the converter to recharge the dip in voltage. At 0.3 sec, the DC link voltage is restored to 600 V. The DC link voltage is regulated at the described value of 600 V.

From the Figure 10 (b), it is witnessed that the output voltage of the three-phase VSI is retained at the 400 V (RMS) during the variation in the load current. Form the Figure 10 (f) – (h), it is perceived that the THD content of the voltage supplied to the grid is less than 0.57% and it is found less which is stated in the IEEE standard IEEE 519-2014 .

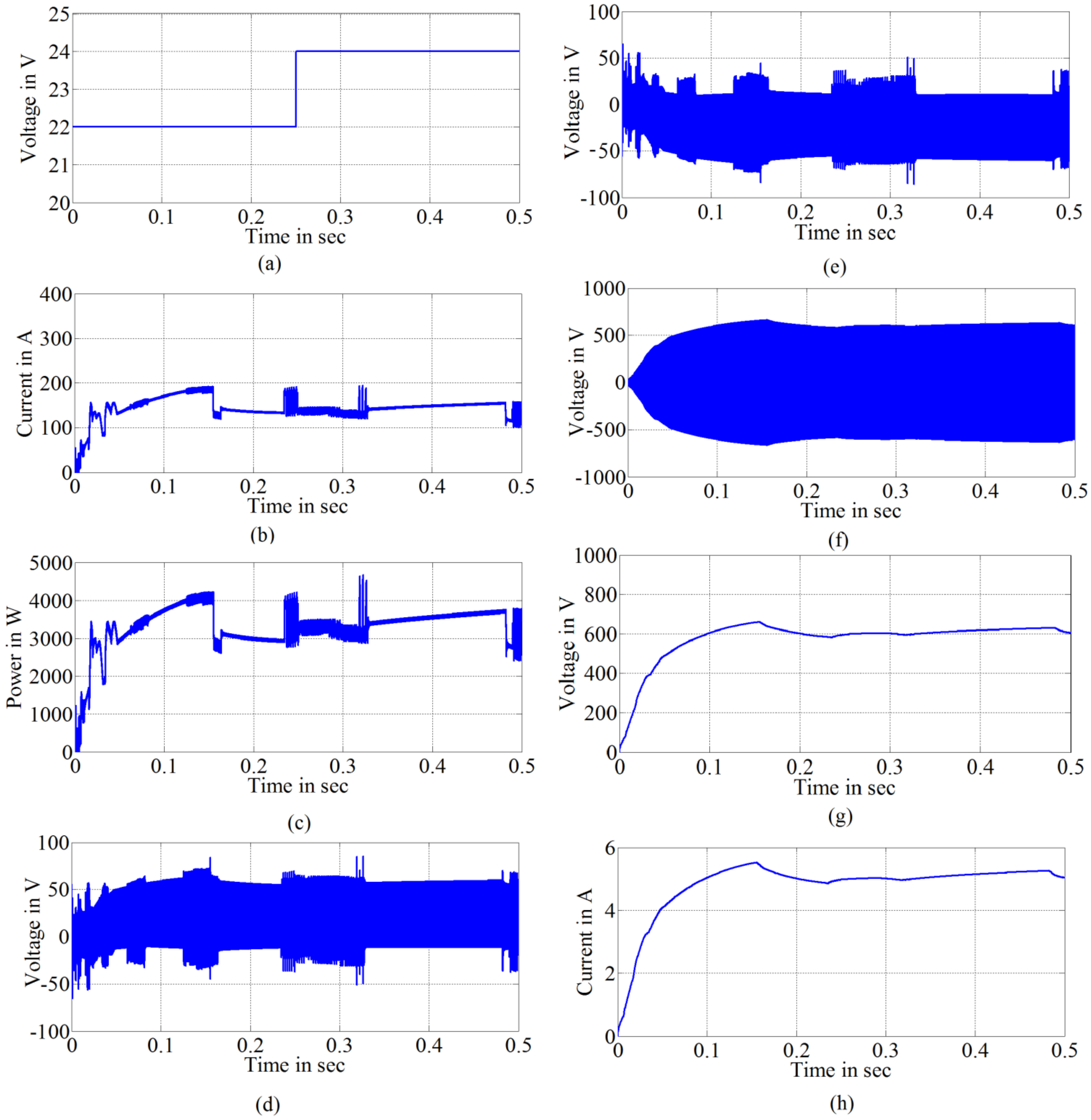

Figure 7. Case 1 Simulation Results: (a) PV array voltage; (b) PV array current; (c) PV Power; (d) Primary 1 Voltage; (e) Primary 2 Voltage; (f) Secondary Voltage; (g) DC Link Voltage; (h) DC link Current.

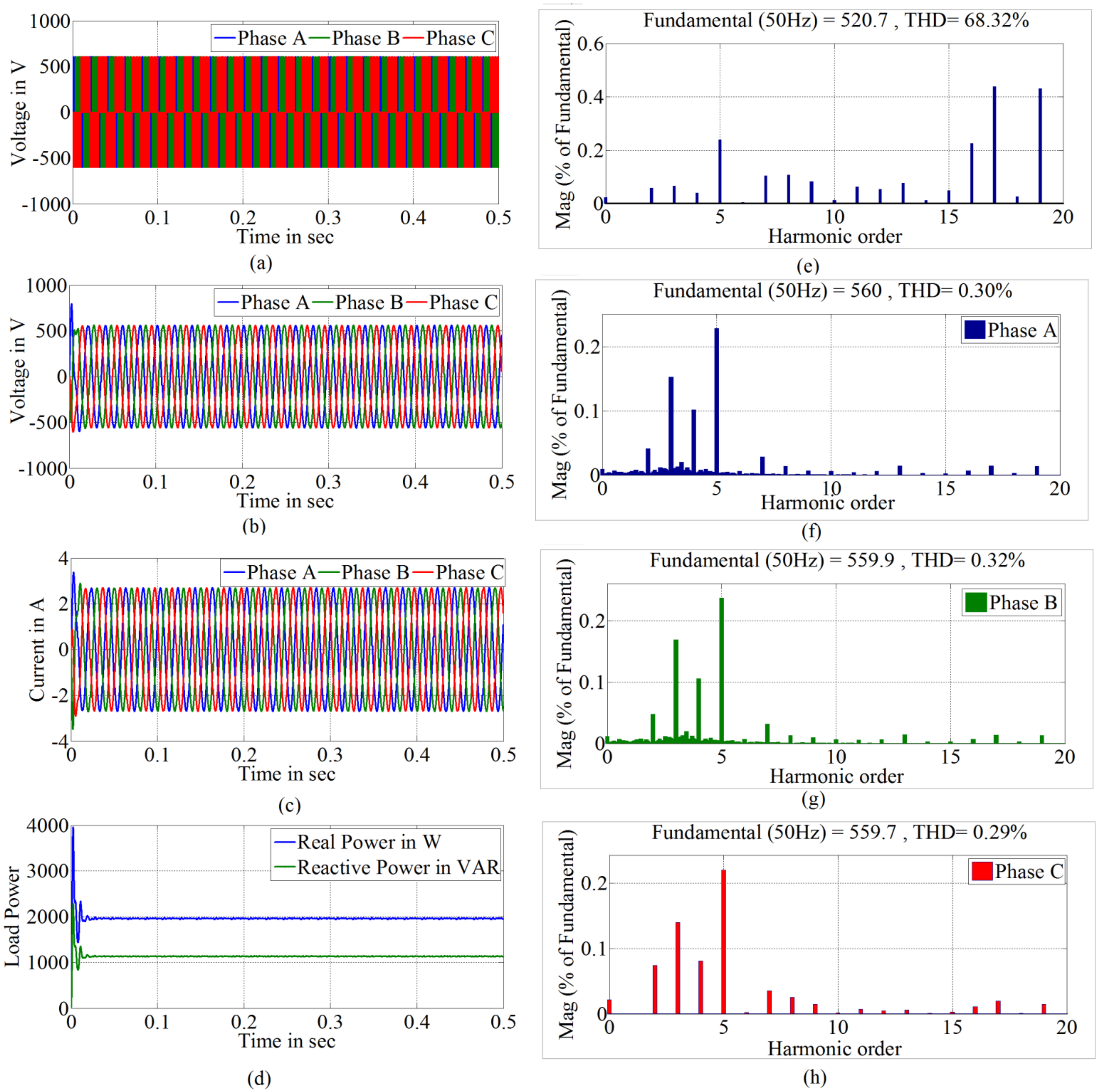

Figure 8. Case 1 Simulation Results: (a) Inverter output voltage without filter; (b) Load voltage; (c) Load current; (d) Real and reactive power of the load ; (e) THD content of the inverter output voltage; (f) THD content of phase A (g) THD content of phase B; (h) THD content of phase C.

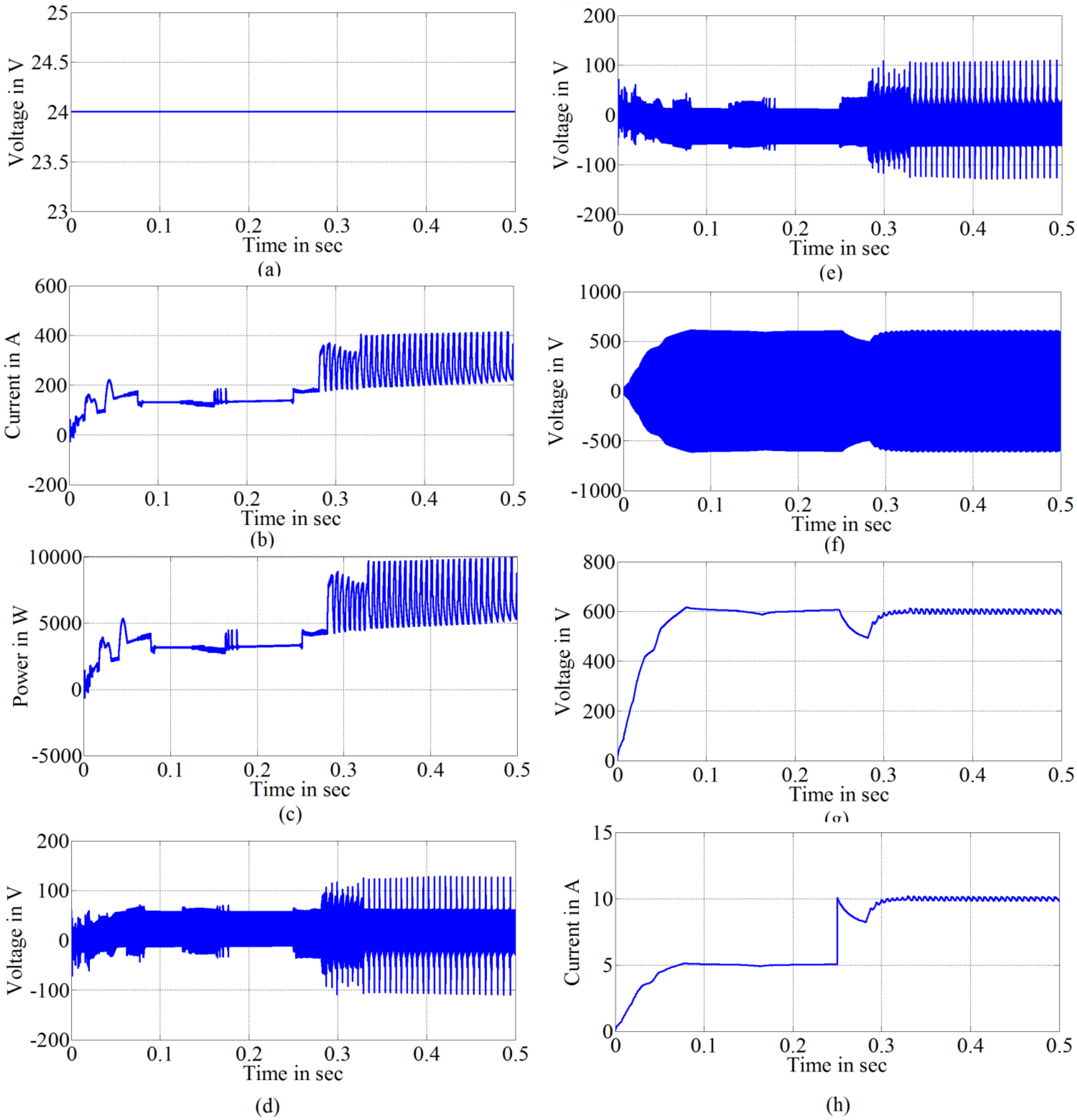

Figure 9. Case 2 Simulation Results: (a) PV array voltage; (b) PV array current; (c) PV Power; (d) Primary 1 Voltage; (e) Primary 2 Voltage; (f) Secondary Voltage; (g) DC Link Voltage; (h) DC link Current.

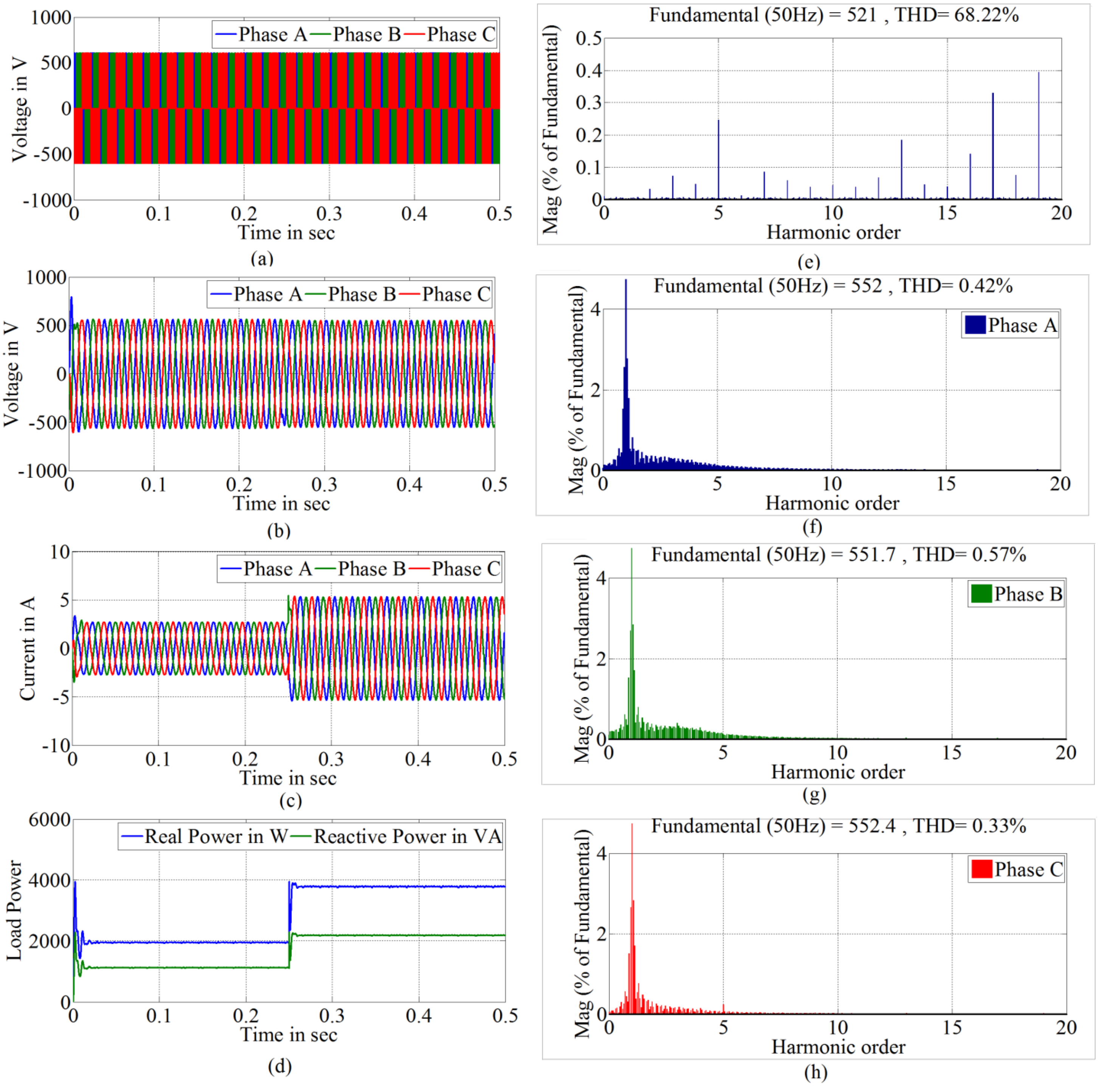

Figure 10. Case 2 Simulation Results: (a) Inverter output voltage without filter; (b) Load voltage; (c) current withdrawn by the load; (d) power withdrawn by the load connected with the grid; (e) THD content of the inverter output voltage; (f) THD content of phase A (g) THD content of phase B; (h) THD content of phase C.

5. Experimental Verification

A 6 kW experimental prototype model has been developed to validate the proposed topology and control strategy. The experimental validation is carried out by applying variable load and variable solar irradiation on the proposed system. Figure 11 depicts the P V array output voltage, PV array output current, primary 1 and primary 2 voltages of the coupled inductor. When the variation in the PV voltage happened the controllers respond to the variation and adjust the duty ratio accordingly to regulate the DC link voltage.

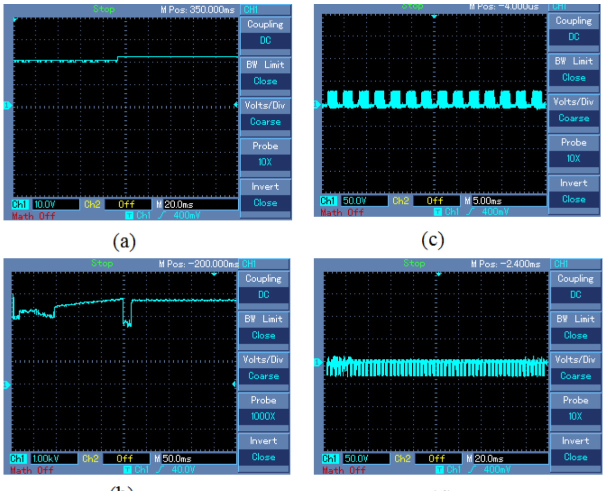
(a) (c)

(b) (d)

Figure 11. Experimental Results: (a) PV array output voltage; (b) PV current; (c) Primary 1 voltage and (d) Primary 2 voltage of the coupled inductor.

Figure 12 depicts the secondary voltage of the coupled inductor, DC link voltage, inverter output voltage before filter, inverter output voltage after filter and load voltage and current of the proposed micro-inverter. From the results, it is concluded that: 1) The MACFFC converter offers high boosting gain reduced DC ripple and duty ratio and 2) The output voltage of the three-phase VSI is not affected with sudden increase in the PV array output voltage and load current. In Table 2, the statistical analyses of conventional and studied dual boost MACFFC derived micro-inverters are presented to confirm the power transfer capability under different PV power generation. The ideal rating of the different topology of the micro-inverters are considered for the comparison.

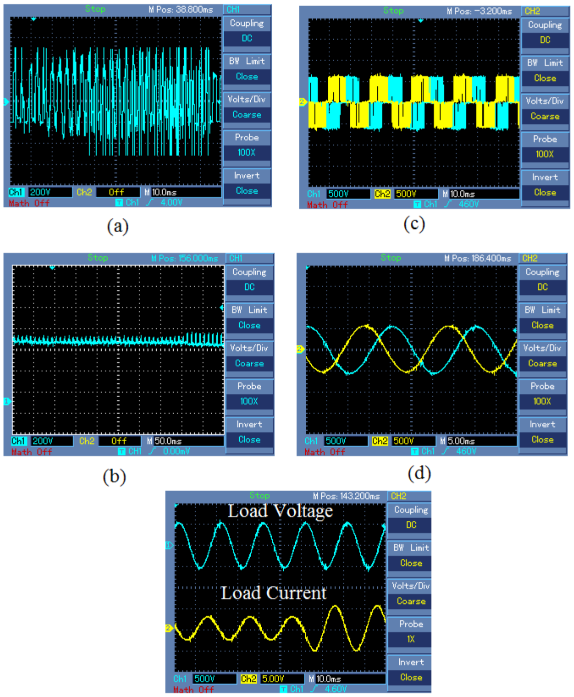

(a) (c)

(b) (d)

(e)

Figure 12. Experimental Results: (a) Secondary Voltage; (b) DC link voltage ; (c) Two phases of the inverter output voltage before filter; (d) Two phase of inverter output voltage after filter and (e) load voltage and current.

From the numerical investigation, it is found that the proposed MACFFC derived three-phase micro-inverter provides high boosting gain with low duty ratio and high efficiency than the other conventional micro-inverter.

Table 2 Numerical presentation of the results obtained from the simulation

PV array Voltage	Duty Ratio	High step-up DC-DC Converter fed Micro-Inverter [5]		Conventional ACFFC derived Micro-Inverter [16]		Studied MACFFC derived Micro-Inverter	
		Output Voltage	**Gain**	**Output Voltage**	**Gain**	**Output Voltage**	**Gain**
24	0.1	244	10.16	320	13.33	346	14.41
24	0.2	279	11.62	360	15	396	16.5
24	0.4	384	16	480	20	496	20.66
24	0.6	594	24.75	720	30	810	33.75
24	0.8	1224	51	1440	60	1520	63.33
24	0.9	2484	103.5	2880	120	2950	122.91
P_{PV}		**Efficiency**					
10 %		92.90 %		89.98 %		94.15 %	
25 %		93.65 %		94.15 %		95.41 %	
50 %		94.50 %		95.65 %		96.89 %	
75 %		95.40 %		96.78 %		97.69 %	
100 %		95.71 %		96.85 %		97.80 %	
Number of Passive and Active Components							
MOSFET Switch		7		10		6	
Inductor		3		3		5	
High frequency Transformer		1		-		1	
Coupled Inductor		1		2		-	
Diode		5		2		2	
Capacitors		9		7		7	

6. Conclusion

In this paper, a dual boost MACFFC derived isolated three-phase micro-inverter is presented. The MACFFC offers two-stage step-up for the PV array output voltage when compared with the conventional ACFFC. The active clamp circuit reduces the voltage stress across the high frequency switches. It increases the life span of the power semiconductor switches. Moreover, it also enhances the power transfer capability, reliability and amplifying ability of the system. The different operating modes of the proposed micro-inverter are presented in a clear and comprehensive way. The ANN based grid side control and voltage control loop ensures the stability of the proposed system under different operating conditions. The simulation and experimental results have proved the theoretical and practical implementation of the proposed three-phase micro-inverter.

Reference

[1] Kjaer, S.B., Pedersen, J.K., and Blaabjerg, F., “A review of single-phase grid-connected inverters for photovoltaic modules,” IEEE Transaction on Industrial Applications, Vol. 41, No.5, pp. 1292-1306, 2005.

[2] Mukhtiar Singh, Vinod Khadkikar, Ambrish Chandra and Rajiv K. Varma., “Grid Interconnection of Renewable Energy Sources at the Distribution Level With Power-Quality Improvement Features,” IEEE Transaction on Power Delivery, Vol. 26, No. 1, pp. 307-315, 2001.

[3] Ramasamy, M., Thangavel, S., “Optimal utilization of PV solar system as DVR (PV-DVR) for a residence or small industry,” Journal of Applied Science and Engineering, Vol. 16, No. 3, pp. 295-304, 2013.

[4] Sankarganesh, R., and Thangavel, S., "Design of A PV Module-Integrated Ćuk Converter Based Isolated Dual Boost Micro-inverter" Journal of Testing and Evaluation, Vol.44, No.3, pp. 1131-1147, 2014.

[5] Geetha, P., and Ravi, S. "PV Module Integrated Dual Boost Isolated DC-DC Converter fed Three-Phase Micro-Inverter," Journal of Testing and Evaluation, Vol. 46, No.3, pp. 1145–1157, 2018.

[6] Bin Gu, H., Jason Dominic, Jih-Sheng Lai, Chien-Liang Chen, Thomas LaBella and Baifeng Chen, "High Reliability and Efficiency Single-Phase Transformerless Inverter for Grid-Connected Photovoltaic Systems," IEEE Transaction on Power Electronics, Vol. 28, No.5, 2013, pp. 2235-2245, 2011.

[7] Sara Eftekharnejad, Gerald Thomas Heydt and Vijay Vittal, "Optimal Generation Dispatch With High Penetration of Photovoltaic Generation," IEEE Transaction on Sustainable Energy, Vol. 6, No. 3, pp. 1013-1020, 2015.

[8] Kai Sun, Li Zhang, Yan Xing, and Josep M. Guerrero "A Distributed Control Strategy Based on DC Bus Signaling for Modular Photovoltaic Generation Systems with Battery Energy Storage," IEEE Transactions on Power Electronics, Vol. 26, No. 10, pp. 3032-3045, 2011.

[9] Manimekalai, P., Harikumar, R., and Raghavan, S., "SOGI Algorithm-Based Shunt Active Power Filter for Grid Integration of Photovoltaic Systems," Journal of Circuits, Systems and Computers, Vol. 25, No. 5, 2016.

[10] Ramasamy, M., and Thangavel, S., "Optimal Utilization of Hybrid Wind–Solar System as DVR for Voltage Regulation and Energy Conservation," Journal of Circuits, Systems and Computers, Vol. 23, No. 5, 2014.

[11] Minjie Chen, Khurram K. Afridi and David J. Perreault, "A Multilevel Energy Buffer and Voltage Modulator for Grid-Interfaced Micro-Inverters," IEEE Trans. on Power Electronics, Vol. 30, No. 3, pp. 1203-1219, 2015.

[12] Tacca, H.E., "Power factor correction using merged flyback-forward converters," IEEE Transactions on Power Electronics, Vol. 15, No. 4, pp. 585 – 594, 2000.

[13] Vasav Gautam, and Parthasarathi Sensarma, "Enhancing the Voltage Gain of a Flyback Converter Using Leakage Energy," IEEE Transactions on Industrial Electronics, Vol. 54, No.5, pp. 4717-4727, 2018.

[14] Lin Chen, Haibing Hu, Qian Zhang, Ahmadreza Amirahmadi and Issa Batarseh, "A Boundary-Mode Forward-Flyback Converter With an Efficient Active LC Snubber Circuit," IEEE Transactions on Power Electronics, Vol. 29, No. 6, pp. 2944-2958, 2014.

[15] Haibing Hu, Souhib Harb, Nasser H. Kutkut, John Shen, Z., and Issa Batarseh "A Single-Stage Micro-inverter Without Using Electrolytic Capacitors," IEEE Transaction on Power Electronics, Vol. 28, No. 6, pp. 2677-2687,2013.

[16] Wuhua Li, Lingli Fan, Yi Zhao, Xiangning He, Dewei Xu and Bin Wu "High-Step-Up and High-Efficiency Fuel-Cell Power-Generation System with Active-Clamp Flyback–Forward Converter," IEEE Transactions on Industrial Electronics, Vol. 59, No.1, pp. 599-610, 2012.

[17] Milad Keshani, Ehsan Adlib and Hosein Farzanehfard, "Micro Inverter based on single ended primary inductance converter topology with an active clamp power decoupling," IET Power Electronics, Vol. 11, No.1, pp. 73-81, 2017.

[18] Tirthasarathi Lodh, Nataraj Pragallapati and Vivek Agarwal, "An Improved Control Scheme for Interleaved Flyback Converter based Micro-Inverter to Achieve High Efficiency," IEEE 1st International Conference on Power Electronics, Intelligent Control and Energy Systems (ICPEICES), Delhi, India, pp. 1-6, 2017.

[19] Ming-Cheng Chen, Chun-Yu Yang, Chien-Yu Lin and Huang-Jen Chiu, "Highly efficient isolated solar micro-inverter," IECON 2016 - 42nd Annual Conference of the IEEE Industrial Electronics Society, 23-

26 Oct 2016, Florence, Italy, pp. 3070-3074, 2017.